Greater role for Atlantic inflows on sea-ice loss in the Eurasian Basin of the Arctic Ocean

Igor V. Polyakov[1*], Andrey V. Pnyushkov[2], Matthew B. Alkire[3], Igor M. Ashik[4], Till M. Baumann[1], Eddy C. Carmack[5], Ilona Goszczko[6], John Guthrie[3], Vladimir V. Ivanov[7], Torsten Kanzow[8], Richard Krishfield[9], Ronald Kwok[10], Arild Sundfjord[11], James Morison[3], Robert Rember[2], Alexander Yulin[4]

1 *International Arctic Research Center and College of Natural Science and Mathematics, University of Alaska Fairbanks, 930 Koyukuk Drive, Fairbanks, AK, 99775, USA*

2 *International Arctic Research Center, University of Alaska Fairbanks, 930 Koyukuk Drive, Fairbanks, AK, 99775, USA*

3 *Polar Science Center, Applied Physics Lab, University of Washington, 1013 NE 40th Street, Seattle, WA 98105, USA*

4 *Arctic and Antarctic Research Institute, 38 Bering Street, St. Petersburg, 199397, Russia*

5 *Institute of Ocean Sciences, Fisheries and Oceans Canada, 9860 West Saanich Road, Sidney, BC, V8L 4B2, Canada*

6 *Institute of Oceanology, Polish Academy of Sciences, Powstancow Warszawy 55, 81-712 Sopot, Poland*

7 *International Arctic Research Center, University of Alaska Fairbanks, 930 Koyukuk Drive, Fairbanks, AK, 99775, USA, Hydrometeorological Center of Russia, 11-13, B, Predtechensky per., Moscow, 123242, Russia and Arctic and Antarctic Research Institute, 38 Bering Street, St. Petersburg, 199397, Russia*

8 *Alfred-Wegener-Institute, Helmholtz Centre for Polar and Marine Research, Bussestraße 24, 27570 Bremerhaven, and Department of Physics and Electrical Engineering, Bremen University, Otto-Hahn Allee, 28334 Bremen, Germany*

9 *Woods Hole Oceanographic Institution, 22 Water St, Woods Hole, MA 02543, USA*

10 *Jet Propulsion Laboratory, California Institute of Technology,4800 Oak Grove Drive Pasadena, CA 91109, USA*

11 *Norwegian Polar Institute, Fram Centre, N-9296 Tromsø, Norway*

[*]Corresponding author: Igor Polyakov, 907-474-2686, igor@iarc.uaf.edu

Arctic sea-ice loss is a leading indicator of climate change and can be attributed, in large part, to atmospheric forcing. Here we show that recent ice reductions, weakening of the halocline, and shoaling of intermediate-depth Atlantic Water layer in the eastern Eurasian Basin have increased winter ventilation in the ocean interior, making this region structurally similar to that of the western Eurasian Basin. The associated enhanced release of oceanic heat has reduced winter sea-ice formation at a rate now comparable to losses from atmospheric thermodynamic forcing, thus explaining the recent reduction in sea-ice cover in the eastern Eurasian Basin. This encroaching "atlantification" of the Eurasian Basin represents an essential step toward a new Arctic climate state, with a substantially greater role for Atlantic inflows.

Over the last decade, the Arctic Ocean has experienced dramatic losses of sea-ice loss in the summers, with record-breaking years in 2007 and 2012 for both the Amerasian Basin and the Eurasian Basin (EB). More remarkably, the eastern EB has been nearly ice-free (<10 % ice coverage) at the end of summer since 2011 (Fig. 1). Most sea ice-mass loss results from summer solar heating of the surface mixed layer (SML) through cracks in the ice and open water, and consequent melting of the lower surface of the ice (*1-3*). Heat advected into the EB interior by Atlantic water (AW) generally has not been considered an important contributor to sea-ice reduction, due to effective insulation of the overlying cold halocline layer (CHL) (*4*) that separates the cold and fresh SML and pack ice from heat carried by the warm and saline AW.

There are, however, reasons to believe the role of AW heat in sea-ice reduction is not negligible, and may be increasingly important (*5*). Nansen (*6*) identified the importance of warm (temperature >0 °C) and salty intermediate-depth (150-900 m) AW in establishing the thermal state of the Arctic Ocean. Later studies demonstrated that AW is transported cyclonically (counter-clockwise) along the deep Arctic basin margins (*7-10*), carrying enough heat, if released, to melt the Arctic sea ice many times over. Observations from the 1990s and 2000s documented two warm, pulse-like AW temperature anomalies on the order of 1 °C (relative to the 1970s), entering the Arctic through Fram Strait and occupying large areas of the Arctic Ocean (*11-14*). The strength of the 2000s warming peaked in 2007/08, with no analogy since the 1950s (*14*). This AW warming has slowed slightly since 2008 (Fig. 2c).

Strong stratification, which is found in most of the Arctic Ocean, prevents vigorous ventilation of the AW. One notable exception is the western Nansen Basin, north and

77 northeast of Svalbard, where proximity to the sources of inflowing AW makes possible
78 significant interactions between the SML and the ocean interior (*5*). Specifically, weakly
79 stratified AW entering the Nansen Basin through Fram Strait is subject to direct
80 ventilation in winter, caused by cooling and haline convection associated with sea ice
81 formation (*15*). This ventilation leads to the reduction of sea-ice thickness along the
82 continental slope off Svalbard (*16, 17*). In the past, these conditions have been limited to
83 the western EB, since winter ventilation of AW in the eastern EB was constrained by
84 stronger stratification there. However, newly acquired data show that conditions
85 previously only identified in the western Nansen Basin now can be observed in the
86 eastern EB as well. We call this eastward progression of the western EB conditions the
87 "atlantification" of the EB of the Arctic Ocean.

88 **Overview of sea ice state**

89 The progressive decline in sea ice coverage of the Arctic Ocean during the satellite era, at
90 13.4 % per decade during September (*18*), has been accompanied by decreases in average
91 sea ice thickness of at least 1.7 m in the central Arctic (*19, 20*). In the region of the
92 eastern EB defined by the polygon in Fig. 1a, the local changes since 2003 have also been
93 substantial. With the northward retreat of multiyear sea ice cover (*21*), coverage within
94 that polygon is now dominated by seasonal ice, either advected from the east and south,
95 or produced locally. Mean September ice coverage has been <10 % of the total area
96 during the last five years, portending ice-free summers in coming years if current sea ice
97 trends prevail. Annual open water coverage has increased from less than one month to
98 more than three months in recent years (Fig. 1b); these longer ice-free periods,
99 maintained by atmospheric and ocean conditions, increase direct air-ocean interactions

100 (momentum and energy exchanges). Available satellite estimates of ice thickness in this
101 region—typically sparse—suggest a concurrent trend, leading to an overall thinning of
102 ~0.5 m (in March) from 2003 through 2015 (Fig. 1c). Satellite records show that this
103 pattern continued in 2016, with less extensive (compared with record minimum)
104 December sea-ice extent in the Kara and Barents Seas (22).

105 **Role of atmospheric thermodynamics in sea-ice decline**

106 Arctic-wide warming is evident from surface air temperature trends ranging between 0.1
107 and 0.3 °C per decade for the period 1984-2012 (*23*). Surface air temperature trends from
108 weather stations and ERA-Interim reanalysis data for the Laptev Sea and eastern EB
109 region far exceed observed average Arctic regional trends (Fig. S1a-c), consistent with
110 recently enhanced sea-ice decline. The net atmospheric thermodynamic impact on sea ice
111 cannot be quantified using surface air temperature records alone, as changes in this
112 parameter omit thermodynamic forcing due to additional atmospheric processes.

113 Fortunately, records are available for fast-ice (motionless seasonal sea ice anchored to
114 the shore, which melts and re-freezes each year) thickness, providing a measure of nearly
115 pure atmospheric thermodynamic forcing over the broad, shallow Siberian shelves, where
116 the impact of advected or seasonally stored oceanic heat is negligible. Records from five
117 locations along the Laptev Sea coast (Fig. S1e) have been used to construct a composite
118 time series showing that increased melting in the eastern EB/Laptev Sea region during
119 the last decade accounted for ~18 cm of ice thickness loss (Fig. S1d). This estimate is
120 statistically significant (using the Student t test), and suggests that atmospheric
121 thermodynamic forcing plays an important role in reducing EB sea-ice coverage.

Recent atlantification of the Eurasian Basin

Observations from 2013 to 2015 using oceanographic moorings (Fig. S2) and drifting Ice-Tethered Profiler buoys (ITPs) (*3, 24*) provide evidence that the eastern EB is in a transition to conditions similar to the western Nansen Basin. Mooring observations over the central Laptev Sea slope sustained since 2002 reveal anomalously strong seasonal signals in the subsurface layers during recent years (Figs. 2c and S3). In particular, the enhanced seasonal signals in the winters of 2013/14 and 2014/15 are associated with warming (Fig. 2b, c) and shoaling of the AW layer (Fig. 2b, d), and weakening of the stability of the CHL and upper pycnocline (~50-150 m, Fig. 2b). As a result, the strength of the seasonal signal, as shown by wavelet analyses (Figs. 2d and S3), was intensified. The AW layer's seasonal temperature range at the $M1_4$ mooring site increased from 0.2-0.3 °C in 2004/07 (*25*) to over 1 °C in 2013/15 (Fig 2b). Shoaling of the AW upper boundary was also substantial, rising from 140 m in 2003/04 to 100 m in winter 2014/15 and even to 85 m in winter 2013/14 (Fig. 2d), with direct consequences for winter entrainment of AW in the upper ocean.

Observations from the widely distributed array of moorings and ITPs can be used to place measurements from the $M1_4$ mooring location in a basin-wide context (Fig. 3). Temperature and salinity distributions provided by ITP-93, which drifted along the Lomonosov Ridge separating the Amerasian and Eurasian basins, are distinct from those provided by other instruments (Fig. 3). They show a stable SML and CHL (white and black lines in Fig. 3c; see Supplementary Materials for SML and CHL depth definitions), and lack strong depth variability throughout the record. The ITP-93 record shows high values for Brunt-Väisälä frequency (a measure of water column stability) at roughly 25-

50 m depth from the beginning (September 22, 2015) to the end (April 22, 2016) of the record, thus providing further evidence for minimal mixing along the eastern flank of the EB in recent years (Fig. 3c).

ITP-57 drifted within the central Amundsen Basin in 2013. Its record shows, in contrast, clear signs of winter ventilation associated with gradual cooling and erosion of the CHL from November/December through April, weakening stratification at the base of the SML, and a decrease in Brunt-Väisälä frequency in the CHL during March-April of 2013 (Fig. 3d). Data from ITP-37 (not shown), which drifted in the same region in 2009/10, indicated that the transfer of heat from the upper pycnocline (~65-100 m) to the SML is highest in winter, with an average heat loss of 3–4 W m^{-2} between January and April (*14*). This analysis has also suggested the increased heat transfer from the AW to the SML in winter is likely caused by a combination of brine-driven convection, associated with sea-ice formation and larger vertical velocity shear below the base of the SML, which is enhanced by strong winter storms and a more mobile ice cover.

A year-long 2013/14 ITP-74 record from the central Nansen Basin showed deepening of the SML to ~130 m and disappearance of the CHL driven by winter convection in March-April 2014, when the buoy was passing westward to the north of Franz Josef Land (Fig. 3b). A seasonally ventilated halocline was also found in this region during a Russian ice drift station NP-35 in 2007/08 (*5*) and in earlier observations (*26, 27*). The disappearance of the CHL was also observed in the central Amundsen Basin in the mid-1990s (*28*). This was explained by a deficit of freshwater in the region, due to a diversion of Siberian river waters further eastward along the coast that was driven by changes in the atmospheric circulation.

168 The deep winter ventilation and the disappearance of the CHL in the eastern EB
169 (eastward from Severnaya Zemlya, >90°E) at several mooring sites in 2013-15, however,
170 are unprecedented (Figs. 3a, 4). Significant changes in seasonal heat content Q (see
171 definition in Supplementary Materials), driven by surface cooling and salinification
172 during winter sea-ice formation, occurred in the upper 130-m layer at M3e, $M1_3$, $M1_6$,
173 and M6b mooring sites. If this trend persists, convectively-driven winter development of
174 the deep (>80 m) SML, combined with ventilation of the upper 130-m ocean and
175 associated disappearance of the CHL would represent a fundamental change, with the
176 eastern EB water column structure becoming less stratified and susceptible to further
177 mixing.

178 **Role of oceanic heat in sea-ice decline**

179 Figure 4 addresses the consequences of these changes for upward AW heat transfer.
180 Seasonal (winter-to-summer) cooling in the CHL and upper pycnocline (65-130 m, see
181 definition in Supplementary Materials) is quantified using linear trends in Q. These
182 trends (Wm^{-2}) characterize the rate of change in Q, and are equivalent to a divergent heat
183 flux F_h (see definition in Supplementary Materials). Note that AW is the major source of
184 heat for the layer underlying the CHL in this part of the Arctic Ocean. The seasonal mean
185 F_h through the CHL and upper pycnocline inferred from these trends varies from 3.3 to
186 24.1 Wm^{-2} (Table 1; for reference, 1 Wm^{-2} over a single year is equivalent to ~10 cm of
187 ice loss).

188 Another potential contributor to the observed change in Q may be the lateral advection
189 of heat. We argue, however, that the in-phase seasonal maxima and minima of wavelet
190 transforms of Q as provided by all moorings (Fig. S4), and the lack of any lag between Q

191 calculated within separate overlying depth layers (not shown), each strongly suggest the
192 observed winter ventilation of the CHL and upper pycnocline is driven by surface cooling
193 and sea-ice formation—and not by lateral advection. Additional support for this statement
194 comes from the wavelet analysis of Q records—not just from moorings $M1_3$ and $M1_6$, but
195 from all six moorings deployed across the EB continental slope during 2013/15 (see
196 Supplementary Materials for data description)—showing in-phase seasonal variations
197 (not shown). The very different speeds of water transports across the slope, ranging from
198 13 cm/s (measured by 250-700 m shallow moorings) to 1-2 cm/s (measured at 2700 m
199 and deeper mooring locations) make the in-phase pattern of the seasonal signal at all
200 moorings impossible to explain using the advective mechanism. Moreover, the $M1_6$
201 mooring was placed in the ocean interior, well away from intense heat transports
202 associated with the near-slope boundary current, and yet data from this mooring yielded
203 estimates for F_h consistent with estimates from other moorings deployed on the eastern
204 EB continental slope.

205 Spatial averaging yields a seasonal mean F_h = 12.2±3.8 W m^{-2} for winter 2013/14 and
206 7.5±0.8 Wm^{-2} for winter 2014/15 (Fig. 4 and Table 1). These inferred F_h values exceed
207 previous estimates for upward heat fluxes of O[3-4] Wm^{-2}, derived from 2007/08
208 microstructure observations over the Laptev Sea slope (*33*) and 2009/10 ITP-37
209 observations in the central Amundsen Basin (*14*) (Table 1), with new estimates for the
210 same region being 2-4 times higher. We thus argue that AW shoaling, weakening of
211 stratification, and warming of the upper pycnocline have led to seasonal upward AW heat
212 fluxes never before observed in the eastern EB.

213 The inferred heat fluxes are equivalent to 54 and 40 cm reductions in ice growth over

214 the 2013/14 and 2014/15 winter seasons, respectively, in the eastern EB (time intervals
215 for seasons as defined by wavelet analysis, Fig. S4). The 2-4 fold increase in F_h since
216 2007/08 explains up to 18-40 cm of sea-ice loss due solely to an increase in upward AW
217 heat transport. These estimates are comparable to or even exceed ~18 cm in sea-ice loss
218 attributed to atmospheric thermodynamic forcing, and partially explain eastern EB sea-
219 ice loss in recent years.

220 **Sources of EB warm-water anomalies**

221 Divergence of the Ekman transport (called Ekman pumping, see definition in
222 Supplementary Materials) may be a local factor, which can cause shoaling of AW and its
223 ventilation. However, our estimates suggest that Ekman pumping can explain only a
224 1.5 m seasonal shoaling of the AW, and therefore does not contribute substantially to the
225 anomalous state of the eastern EB in recent years (Fig. S5).

226 Geochemical observations demonstrated that fresh shelf waters cross the Laptev Sea
227 shelf break primarily at the Lomonosov Ridge–continental slope junction (*35*). Thus,
228 while variations in atmospheric forcing have been shown to affect the storage or release
229 of shelf waters (*35*) that impact stratification in the Amundsen Basin (*28*), such variations
230 likely play only a minor role in the recent changes observed in the eastern EB.

231 We thus conclude that the source of changes associated with the AW in the eastern EB
232 lies in processes beginning in upstream locations—namely, in Fram Strait and the
233 western EB north of Svalbard. Similar to eastern EB observations, the vertical
234 temperature difference in the upper ocean (>250 m) has been reduced in the area
235 northeast of Svalbard since 2004 (Fig. S6d, e) due to warming in the upper part of the
236 water column, mostly during winter. This trend is not present in data from Fram Strait,

where the temperatures at both 75 and 250 m have changed very little (Fig. S6b, c).

One important difference between the eastern Fram Strait and the area northeast of Svalbard is that the eastern (inflow) side of Fram has been essentially ice-free year-round throughout recent history, while the slope north of Svalbard—beyond the Yermak Plateau—has traditionally been ice-covered most of the year. In recent decades, larger areas north of Svalbard have been ice-free for longer periods, primarily due to a contemporary increase in temperature of the AW inflow (*16, 17*), similar to the response in the Barents Sea to increased AW heat input there (*36*). During these extended ice-free periods over the slope north of Svalbard, enhanced local wind-driven generation and breaking of internal waves would be expected, as has been observed elsewhere in the Arctic (*37*). As a result, increased sub-surface vertical mixing would tend to reduce the temperature gradient, and increase Q above the temperature maximum in the AW inflow core—consistent with Fig. S6d, e. Additionally, the longer ice-free season over a larger area allows more solar radiation to be absorbed in the upper ocean, thus compensating to some degree for the increased local heat loss to the ice and atmosphere.

Discussion

This study provides evidence that the eastern EB is now in transition to conditions previously unique to the western Nansen Basin—an extension of over 1500 km along the AW pathway from Fram Strait, as far as 125°E. The term ‘atlantification’ is applied to the northward movement of sea ice in the Barents Sea, with attendant reductions in stratification, increased vertical mixing, and altered primary production (*38, 39*). The recent extension of “atlantification” far into the EB, and the suite of associated processes, is shown conceptually in Fig. 5. The major driver for these changes is a powerful

combination of processes associated with declining sea-ice cover and weakening of stratification in the layers over AW. Gradual weakening of stratification in the eastern EB halocline began in at least the 1970s (*28, 40*), providing the necessary pre-conditioning for a reconstruction of water mass structure. Weaker stratification and shoaling of the AW, together with net loss in ice volume, allow progressively deep winter ventilation in the eastern EB. This ventilation has resulted in enhanced upward AW heat fluxes, key to establishing the diminished sea-ice cover in the eastern EB during recent years.

Changes associated with "atlantification"—weakened stratification, increased vertical mixing, and sea ice decline—will have dramatic impacts on other geophysical and biogeochemical components of the Arctic Ocean system. These include enhanced atmosphere-ocean interactions (with potential but highly debated mid-latitude consequences; *41*), altered freshwater storage and export patterns within the Arctic Ocean (*42*), intensified shelf-basin exchange (*43*), increased primary production due to increased nutrient supply (*44*), and possibly changing the ocean's response to acidification due to the high buffering capacity of AW (*45*). While specific physical mechanisms involved in sea ice decline and upper ocean ventilation remain under debate (*5*), it is likely that higher-than-normal AW temperatures and salinities in the Nordic Seas, upstream of the Arctic Ocean gateways (*46*), will promote the further eastward "atlantification" of the polar basins. This follows with scenarios for regional ocean state responses to the climate changes proposed in (*47*), and has significant effects for future changes in the Arctic Ocean and its sea-ice cover. The validity of extrapolating trends in the Arctic climate system into the future is impacted, however, by the existence of large-amplitude, high-latitude variability (*48-50*). It is therefore imperative to apprehend how to separate

283 climate trends and variability and to understand their nature, in order to improve accuracy
284 of climate projections.
285

References and Notes

1. D. K. Perovich *et al*. *Ann Glaciol.* **52**, 355-359 (2011).

2. D. K. Perovich *et al*. *Geophys. Res. Lett*. **41**, 2019–2025 (2014).

3. J. M. Toole *et al*. *J. Geophys. Res.* **115**, C10018 (2010).

4. K. Aagaard, L. K., Coachman, E. C. Carmack, *Deep-Sea Res*. **28**, 529-545 (1981).

5. E. C. Carmack *et al*. *Bull. Amer. Meteor. Soc.* **96**(12), 2079-2105 (2015).

6. F. Nansen. *Sci. Results.* **9**, 427 (1902).

7. K. Aagaard, *Rapp. P.-V. Reun. Cons. Int. Explor. Mer.* **188**, 11-22 (1989).

8. B. Rudels, E. P., Jones, L. G. Anderson, G. Kattner, in *The Polar Oceans and Their Role in Shaping the Global Environment: The Nansen Centennial Volume,* AGU Geophysical Monograph vol. **85**, American Geophysical Union, Washington DC, 1994, 33-46 (1994).

9. Y. Aksenov *et al*. *J. Geophys. Res.* **116**, C09017 (2011).

10. A. Pnyushkov *et al*. *Deep-Sea Res. I*. **101**, 80–97 (2015).

11. D. A. Quadfasel, A. Sy, D. Wells, A. Tunik, *Nature*. **350**, 385 (1991).

12. E. C. Carmack *et al*. *Geophys. Res. Lett*. **22**, 1061-1064 (1995).

13. I. V. Polyakov *et al. Geophys. Res. Lett*. **32***,* L17605 (2005).

14. I. V. Polyakov *et al*. *J. Phys. Oceanogr.* **43**, 2142-2155 (2013).

15. V. Ivanov *et al*. *J. Phys. Oceanogr*. **46**, 1437-1456 (2016).

16. V. V. Ivanov *et al. Advances in Meteorology*. **2012**. Article ID 201818. 11 pp. (2012).

17. I. H. Onarheim, L. H., Smedsrud, R., Ingvaldsen, F. Nilsen, *Tellus*. **66**, 23933 (2014).

18. D. G. Vaughan *et al*., In: *Climate Change 2013:* Cambridge University Press,

Cambridge, United Kingdom and New York, NY, USA, pp. 317–382 (2013).

19. R. Kwok, D. A. Rothrock, *Geophys. Res. Lett*. **36**, L15501 (2009).

20. R. Kwok, G. F. Cunningham, *Phil. Trans. R. Soc. A*. **373**, 20140157 (2015).

21. I. V. Polyakov, J. Walsh, R. Kwok, *Bull. Amer. Meteor. Soc.* **93**(2), 145–151 (2012).

22. Sea Ice Prediction Network (SIPN). Post-Season Report, https://www.arcus.org/sipn/sea-ice-outlook/2016/post-season#two (2016).

23. C. Li, B. Stevens, J. Marotzke, *Geophys. Res. Lett*. **42**, 8131–8139, (2015).

24. R. Krishfield, J. Toole, A. Proshutinsky, M.-L. Timmermans, *J. Oceanic and Atmos. Tech.* **25**, (2008).

25. I. A. Dmitrenko, *et al*. *J. Geophys. Res*. **114**, C06010 (2009).

26. B. Rudels, L. G. Anderson, E. P. Jones, *J. Geophys. Res.* **101**, 8807-8821 (1996).

27. B. Rudels, P. Jones, U. Schauer, P. Eriksson, *Polar Research*. **23**(2), 181–208 (2004).

28. M. Steele, T. Boyd, *J. Geophys. Res. - Oceans*. **103**(C5), 10419-10435 (1998).

29. L. Padman, T. M. Dillon, *J. Geophys. Res*. **96** (C3), 4769–4782 (1991).

30. M. G. McPhee, T. Kikuchi, J. H. Morison, T. P. Stanton, *Geophys. Res. Lett*. **30**(24), 2274 (2003).

31. A. Sirevaag, I. Fer, *J. Phys. Oceanogr*. **39**, 3049-3069 (2009).

32. I. Fer, R. Skogseth, F. Geyer, *J. Phys. Oceanogr*. **40**(7), 1613-1630 (2010).

33. Y.-D. Lenn, *et al*., *Geophys. Res. Lett*. **36**, L05601 (2009).

34. I. Fer, *Atmos. Ocean. Sci. Lett*. **2**, 148-152 (2009).

35. D. Bauch, D., I. A. Dmitrenko, C. Wegner, J. Hölemann, S. A. Kirillov, L. A. Timokhov, H. Kassens. *J. Geophys. Res*., **114**, C05008,

doi:10.1029/2008JC005062, (2009).

36. M. Årthun, T. Eldevik, L- H. Smedsrud, Ø. Skagseth, R. B. Ingvaldsen, *J. Clim*., **25**, 4736-4743 (2012).

37. L. Rainville, R. A. Woodgate, *Geophys. Res. Lett*. **36**, L23604 (2009).

38. M. Reigstad, P. Wassmann, C. W. Riser, S. Øygardena, F. Reyb, *J. Marine Systems*. **38**, 9–29 (2004).

39. P. Wassmann, et al., In: The Organic Carbon Cycle in the Arctic Ocean. Springer-Verlag Heidelberg-Berlin-New York, pp.101-138 (2004).

40. I. V. Polyakov, *et al*., *J. Phys. Oceanogr*. **40**, 2743–2756 (2010).

41. J. Cohen *et al*., *Nature Geoscience*. **7**, 627-637 (2014).

42. E. C. Carmack, *et al*., *J. Geophys. Res. - Global Biogeochemical Cycles*. **121**, 675-717, doi:10.1002/2015JG003140/full (2016).

43. W. Williams, C. E. Carmack, *Progress in Oceanography*. http://dx.doi.org/10.1016/j.pocean.2015.07.008 (2015).

44. B. A. Bluhm, K. N. Kosobokoba, E. C. Carmack, *Progress in Oceanography*, http://dx.doi.org/10.1016/j.pocean.2015.07.011 (2015).

45. M. Yamamoto-Kawai, F. McLaughlin, E. C. Carmack, *J. Geophys. Res. – Oceans*. **118** (2013).

46. K. M. H. Larsen, C. Gonzalez-Pola, P. Fratantoni, A. Beszczynska-Möller, S. L. Hughes, (Eds.) *ICES Report on Ocean Climate 2015. ICES Cooperative Research Report*. **331**. 79 pp. (2016).

47. K. Aagaard, E. C. Carmack, In The Polar Oceans and Their Role in Shaping the

Global Environment, *Geophys. Monogr. Ser.,* vol. **85**, edited by O. M. Johannessen, R. D. Muench, and J. E. Overland, pp. 5–20, AGU, Washington, D. C., doi:10.1029/GM085p0005 (1994).

48. I. V. Polyakov, *et al*., *Ecol. Applications*. **23**(8), 1745-1764 (2013).

49. A. Proshutinsky, D. Dukhovskoy, M.-L. Timmermans, R. Krishfield, J. L. Bamber, *Phil. Trans. A.* **373**: 20140160. http://dx.doi.org/10.1098/rsta.2014.0160 (2015).

50. R. Zhang, *PNAS*, **112**, 4570-4575 (2016).

51. V. V. Ivanov *et al*., *Deep-Sea Res*. I. **56**, 1-14 (2009).

52. Polyakov, I. V. *NSF Arctic Data Center*. arctic-data.7792.16 (2016).

53. C. Torrence, G. P. Compo, *Bull. Amer. Meteor. Soc.* **79**(1), 61-78 (1998).

54. G. Monterey, S. Levitus, S. NOAA Atlas NESDIS 14, U.S. Gov. Printing Office, Wash., D.C., 96 pp (1997).

55. P. Bourgain, J.-C. Gascard, *Deep-Sea Res. I*, **58**, 745-756 (2011).

Acknowledgments. This study was supported by NSF grants #1203473 and #1249133 (AP, IP, MA, RR, VI), NOAA grant # NA15OAR4310155 (AP, IP, MA, RR, TB, VI) and by the A-TWAIN project, funded by the Arctic Ocean program at the FRAM-High North Research Centre for Climate and the Environment. We thank *Henriksen SS* for help with logistics. The mooring recovery and deployment was a great team effort by all onboard the R/V *Akademik Fedorov* (2013) and R/V *Akademik Tryoshnikov* (2015). We thank our colleagues from the Arctic and Antarctic Research Institute, Russia, particularly V. Vizitov, V. Zaitsev, and E. Morozova, for their help with cruise preparations. All mooring data used in this study are available on the web at https://arcticdata.io/catalog/#view/arctic-data.7792.4 (Ref. *52*).

Author Contributions. All authors participated in data processing and preliminary analysis; AP, IA, IP, RR, and VI carried out statistical analysis of data, RK provided sea-ice information and processing, TK processed Fram Strait data, AS provided processing and analysis for Svalbard mooring data, AY analyzed fast ice thickness data, and TB worked with reanalysis data. All authors contributed to interpreting the data and writing the paper.

Author Information. The authors declare no competing financial interests. Correspondence and requests should be addressed to IP (igor@iarc.uaf.edu).

Tables

Table 1: Estimates of upward heat fluxes F_h (W/m^2).

Region	Topography	Depth level	F_h	Method	Source
Previous estimates, Eurasian Basin					
Yermak Plateau	Steep	Halocline	25	Microstructure profiles	*Ref. 29*
Yermak Plateau	Steep	Ice-ocean interface	22	Turbulent flux buoy	*Ref. 30*
North of Svalbard	Steep	Ice-ocean interface Halocline	*O*[100] *O*[100]	Eddy covariance, Microstructure profiles	*Ref. 31*
North of Svalbard	Slope	Halocline	2-4	Microstructure profiles	*Ref. 32*
Laptev Sea	Slope	Above AW core (>250m)	3	Microstructure profiles	*Ref. 33*
Amundsen Basin	Interior	Upper CHL SML	0.05 0.2	Microstructure profiles	*Ref. 34*
Amundsen Basin	Interior	Between SML and AW core	3-4	ITP, heat content difference	*Ref. 14*
Estimates from this study, eastern Eurasian Basin					
Eastern EB, off Severnaya Zemlya	Steep slope	Between SML and AW core	5.0-10.3	Heat content difference	M6b mooring
Eastern EB, central Laptev Sea, 125E	Slope	Between SML and AW core	8.4-24.1	Heat content difference	$M1_3$ mooring
Eastern EB, 125E	Interior	Between SML and AW core	6.9-11.2	Heat content difference	$M1_6$ mooring
Eastern EB, off Novosibirskiye Islands	Slope	Between SML and AW core	3.3-9.5	Heat content difference	M3e mooring

Figure legends

Figure 1: Sea ice fraction and thickness in the eastern Eurasian Basin (EB) since 2003. Sampling of the sea ice state within the region (of 0.41×10^6 km^2, defined in (a)) shows a positive trend in annual open water coverage (in months, integrated over a seasonal cycle, (b)), this is accompanied by decreases in mean March ice thickness and monthly mean sea ice coverage in (c) (measured as fraction of the total area). For the past five summers (2011 thru 2015), the mean September ice coverage has been less than 10 % ice coverage, and seems to be approaching a seasonally ice-free state. Dashed box (in blue) shows the geographic coverage of the map in Fig. 2a, within the Arctic basin. Red dashed line in (a) identifying the Lomonosov Ridge separates the Amerasian and Eurasian basins.

Figure 2: Mooring locations and time series and their wavelet transforms from the mooring site $M1_4$, eastern EB of the Arctic Ocean. (A) Map showing locations of oceanographic moorings. The Gakkel Ridge (GR) divides the EB into the Nansen Basin (NB) and the Amundsen Basin (AB). The Lomonosov Ridge (LR), Novosibirskiye Islands (NI), Severnaya Zemlya (SZ), Franz Joseph Land (FJL), and Makarov Basin (MB) are indicated. Dotted lines show latitudes and longitudes; grey solid lines show depth in meters. (B) Vertical profiles show increasing water temperature (°C) and salinity and decreasing stability expressed as the logarithm of squared Brunt-Väisälä frequency (N^2, s^{-2}, a measure of water column stability) within the Cold Halocline Layer (CHL) and upper pycnocline (~40-150 m) in the 2000s and early 2010s. (C) Composite time series of water temperature (dotted lines for daily, solid lines for monthly means). White segments indicate missing data. (D) Original (light blue) and de-trended (dark blue) time series of the upper Atlantic Water (AW) boundary (defined by 0 °C isotherm, left) and wavelet transforms of de-trended time series (right). In panels with wavelet transforms, 95 % statistical significance and cones of influence are shown by grey lines.

Figure 3: (top) Potential temperature (°C), (middle) salinity, and (bottom) logarithm of N^2 (s^{-2}) from (a) mooring and (b-d) along the Ice Tethered Profiler drifts. White segments indicate missing data. White solid lines show the depth of the surface mixed layer (SML) and black solid lines show the depth of the underlying cold halocline layer (CHL) base; disappearance of the black line signifies disappearance of CHL and ventilation of the

upper ocean.

Figure 4: (left) Depth (m)-time distributions of temperature, T, and (right) time series of heat content, Q, (dotted blue lines = daily, solid blue lines = monthly means, and green dashed line = standard errors) for the 65-130 m layer (see mooring locations in Fig. 2). Maxima and minima of wavelet transforms were used to define the boundary of winter seasons (Fig. S4). These boundaries were used to calculate trends in Q shown by red (winter 2013/14) and orange (winter 2014/15) lines. Slope of trends defines the rate of change of Q in time, which is equivalent to the divergent heat flux F_h (shown in red and orange).

Figure 5: Conceptual model of "atlantification" of the eastern EB continental margin in recent years. The broad arrow extending from the right hand side shows the encroachment of a suite of processes associated with atlantification; these are (1) increased penetration of surface signature of AW (increased flow, heat content or both) into the eastern EB, (2) reduction in ice cover resulting in (3) greater surface heat and moisture flux and (4) increased depth of winter penetrative convection, bringing additional heat and nutrients from AW into the Arctic Surface water and transformation of the permanent cold halocline layer (CHL) to a seasonal halocline. SML and UPP indicate the surface mixed layer and upper permanent pycnocline. WC shows winter convection; red arrows indicate upward heat fluxes. Horizontal red arrows show inflows.

Figures

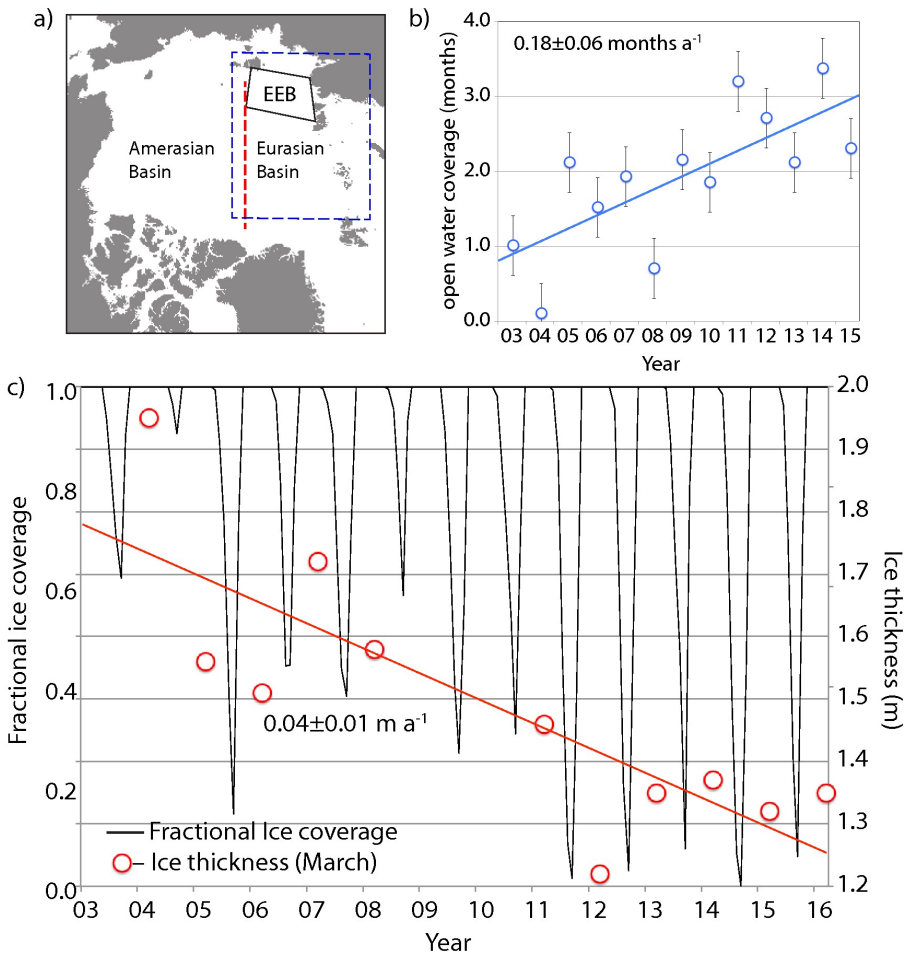

Figure 1: Sea ice fraction and thickness in the eastern Eurasian Basin (EB) since 2003. Sampling of the sea ice state within the region (of 0.41 × 10^6 km^2, defined in (a)) shows a positive trend in annual open water coverage (in months, integrated over a seasonal cycle, (b)), this is accompanied by decreases in mean March ice thickness and monthly mean sea ice coverage in (c) (measured as fraction of the total area). For the past five summers (2011 thru 2015), the mean September ice coverage has been less than 10 % ice coverage, and seems to be approaching a seasonally ice-free state. Dashed box (in blue) shows the geographic coverage of the map in Fig. 2a, within the Arctic basin. Red dashed line in (a) identifying the Lomonosov Ridge separates the Amerasian and Eurasian basins.

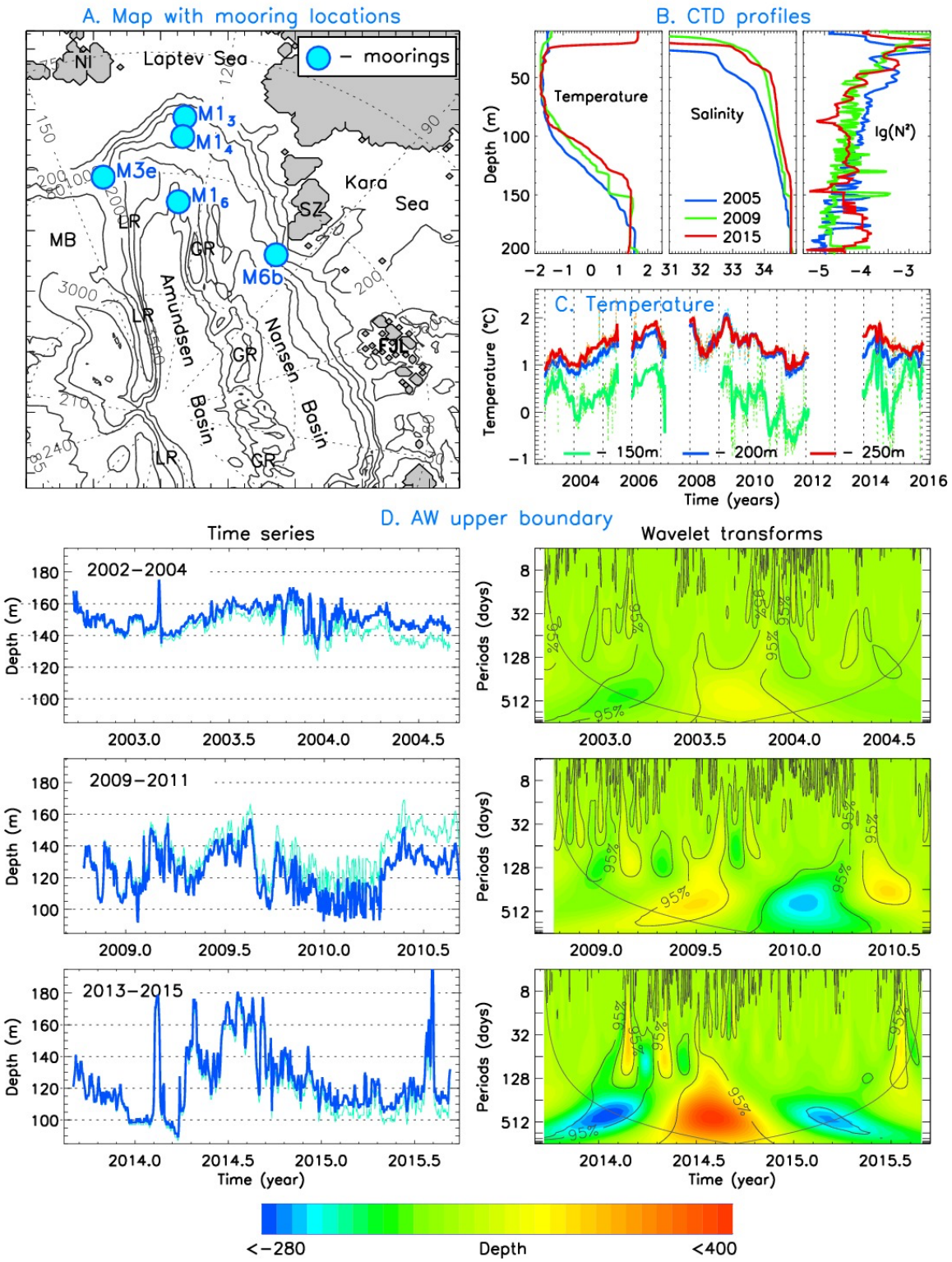

Figure 2: Mooring locations and time series and their wavelet transforms from the mooring site $M1_4$, eastern EB of the Arctic Ocean. (A) Map showing locations of oceanographic moorings. The Gakkel Ridge (GR) divides the EB into the Nansen Basin

(NB) and the Amundsen Basin (AB). The Lomonosov Ridge (LR), Novosibirskiye Islands (NI), Severnaya Zemlya (SZ), Franz Joseph Land (FJL), and Makarov Basin (MB) are indicated. Dotted lines show latitudes and longitudes; grey solid lines show depth in meters. (B) Vertical profiles show increasing water temperature (°C) and salinity and decreasing stability expressed as the logarithm of squared Brunt-Väisälä frequency (N^2, s^{-2}, a measure of water column stability) within the Cold Halocline Layer (CHL) and upper pycnocline (~40-150 m) in the 2000s and early 2010s. (C) Composite time series of water temperature (dotted lines for daily, solid lines for monthly means). White segments indicate missing data. (D) Original (light blue) and de-trended (dark blue) time series of the upper Atlantic Water (AW) boundary (defined by 0 °C isotherm, left) and wavelet transforms of de-trended time series (right). In panels with wavelet transforms, 95 % statistical significance and cones of influence are shown by grey lines.

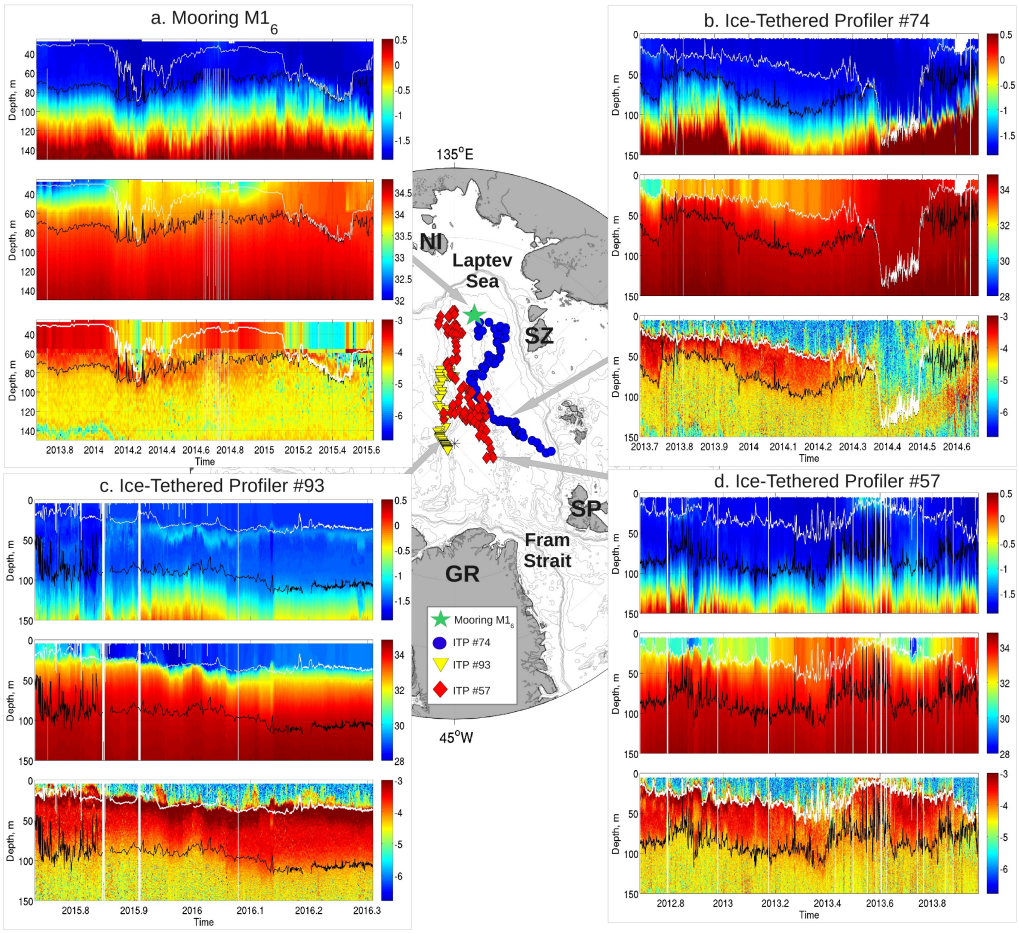

477

478 **Figure 3**: (top) Potential temperature (°C), (middle) salinity, and (bottom) logarithm of
479 N^2 (s^{-2}) from (a) mooring and (b-d) along the Ice Tethered Profiler drifts. White segments
480 indicate missing data. White solid lines show the depth of the surface mixed layer (SML)
481 and black solid lines show the depth of the underlying cold halocline layer (CHL) base;
482 disappearance of the black line signifies disappearance of CHL and ventilation of the
483 upper ocean.

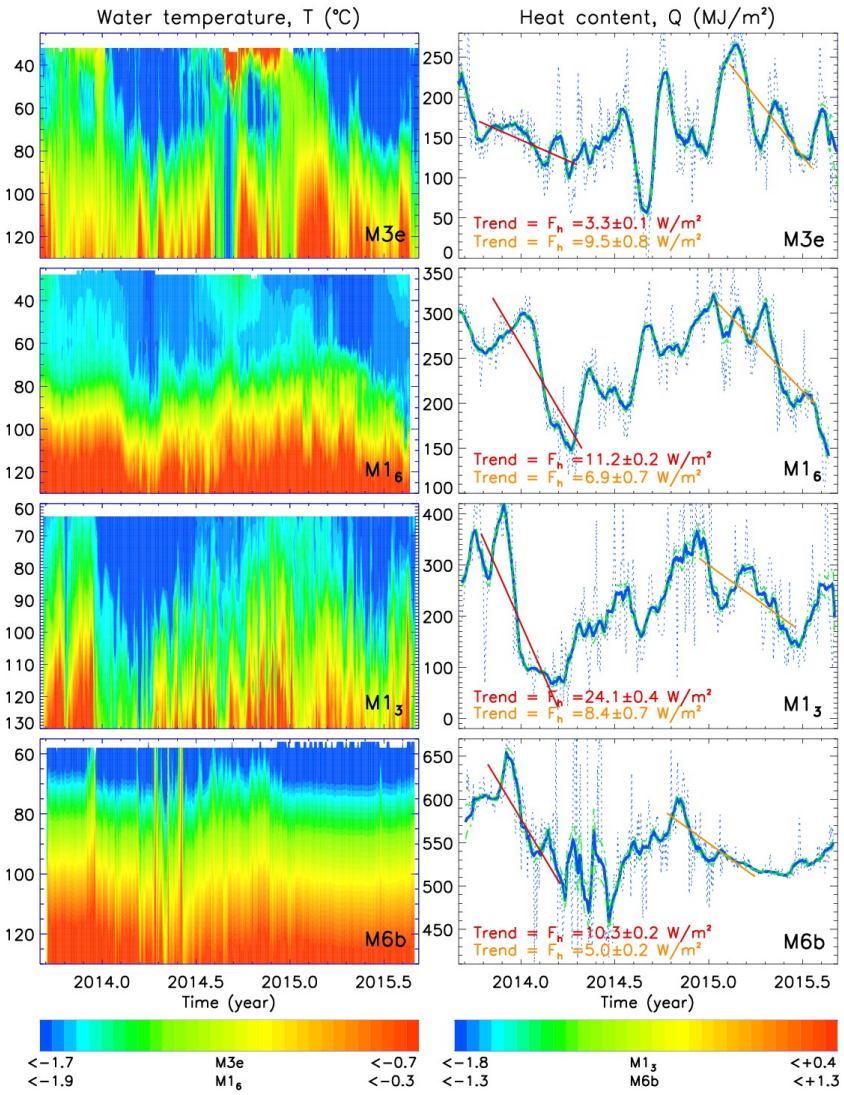

484

485 **Figure 4**: (left) Depth (m)-time distributions of temperature, *T*, and (right) time series of
486 heat content, *Q*, (dotted blue lines = daily, solid blue lines = monthly means, and green
487 dashed line = standard errors) for the 65-130 m layer (see mooring locations in Fig. 2).
488 Maxima and minima of wavelet transforms were used to define the boundary of winter
489 seasons (Fig. S4). These boundaries were used to calculate trends in *Q* shown by red
490 (winter 2013/14) and orange (winter 2014/15) lines. Slope of trends defines the rate of
491 change of *Q* in time, which is equivalent to the divergent heat flux F_h (shown in red and
492 orange).

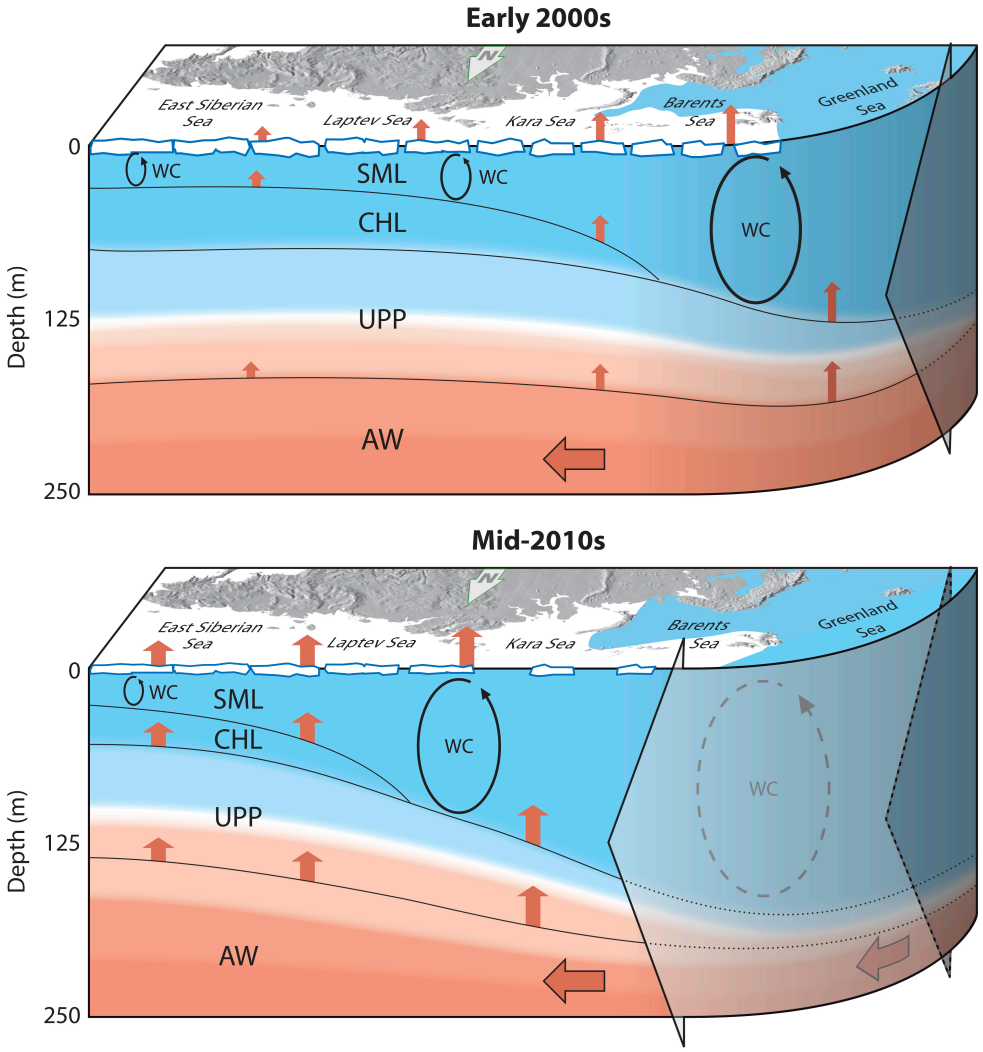

493

494 **Figure 5**: Conceptual model of "atlantification" of the eastern EB continental margin in
495 recent years. The broad arrow extending from the right hand side shows the encroachment
496 of a suite of processes associated with atlantification; these are (1) increased penetration of
497 surface signature of AW (increased flow, heat content or both) into the eastern EB, (2)
498 reduction in ice cover resulting in (3) greater surface heat and moisture flux and (4)
499 increased depth of winter penetrative convection, bringing additional heat and nutrients
500 from AW into the Arctic Surface water and transformation of the permanent cold halocline
501 layer (CHL) to a seasonal halocline. SML and UPP indicate the surface mixed layer and
502 upper permanent pycnocline. WC shows winter convection; red arrows indicate upward
503 heat fluxes. Horizontal red arrows show inflows.

504

Supplementary Materials for

Greater role for Atlantic inflows on sea-ice loss in the Eurasian Basin of the Arctic Ocean

Igor V. Polyakov, Andrey V. Pnyushkov, Matthew B. Alkire, Igor M. Ashik, Till M. Baumann, Eddy C. Carmack, Ilona Goszczko, John Guthrie, Vladimir V. Ivanov, Torsten Kanzow, Richard Krishfield, Ronald Kwok, Arild Sundfjord, James Morison, Robert Rember, Alexander Yulin

correspondence to: igor@iarc.uaf.edu

This PDF file includes:

Materials and Methods

Satellite Observations

Ice concentration fields are those from AMSR. Gridded monthly fields of ICESat and CS-2 ice thickness estimates are those described in *Ref. 20*. The assessed differences between ICESat and various measurements are: 0.14±0.51m (ice draft from moorings), and -0.1±0.42 m (submarine ice draft). Differences between CS-2 and various measurements are: 0.06±0.29 m (ice draft from moorings), 0.07±0.44 m (submarine ice draft), 0.12±0.82 m (airborne electromagnetic profiles), and -0.16±0.87 m (Operation IceBridge).

Mooring Observations

Our analysis utilizes the collection of instrumental observations of ocean temperature and salinity from five moorings distributed in the eastern EB (Fig. 2). Moorings provided CTD (Conductivity-Temperature-Depth) profiles from McLane Moored Profilers (MMP) ($M1_3$ and $M1_6$ moorings only) and SBE-37 CTD time series and SBE-56 temperature time series from fixed depth observations. Mooring schematics with depths of each SBE-37 instrument and depth ranges for MMPs are shown in Supplementary Materials Fig. S2.

The MMP temperature and conductivity calibrated measurement accuracies are ±0.002˚C and ±0.002 mS/cm, respectively. The MMP sampled a vertical profile along a mooring line once per day at a speed of ~25 cm/s with a sampling period of 0.5 s; therefore, the data had a vertical spacing of ~12 cm. SBE-37 and SBE-56 provided 15-min interval records with measurement accuracies of ±0.002˚C and ±0.003 mS/cm for SBE-37 temperature and conductivity and of ±0.002˚C for SBE-56 temperature. All eastern EB moorings were deployed in summer 2013 and recovered in summer 2015 providing full two-year long records for all instruments (with a few exceptions). Two single moorings (M3e and M6b) were located off Novosibirskiye Islands and Severnaya Zemlya. Six moorings formed a cross-slope section along approximately 126°E meridian. Only $M1_3$, $M1_4$, and $M1_6$ from this array, however, were used in this analysis. Despite thinning, the reduced dataset provides a robust description of seasonal variability relevant to the present study. Locations of moorings used in this study are shown in Fig. 2. In addition, at $M1_4$ mooring site observations began in August 2002 thus providing invaluable long-term (with several gaps caused by malfunction of MMP and discontinuity of funding) measurements. Observations started some distance (32-65m depending on mooring) from the surface in order to avoid potential loss of the moorings being trapped and destroyed by ice keels. That limited our ability to define summer SML depths for all moorings. Mooring data used in this study are available on the web, at https://arcticdata.io/catalog/#view/arctic-data.7792.4 (*52*).

In Fram Strait, we utilized long-term observations along the 78°50'N latitude, which extended from the eastern Greenland shelf break (6°51'W) to the western shelf break off Svalbard (8°40'E). We focused our analysis on observations at mooring F3 in the eastern part of this section. This mooring was deployed within the West Spitsbergen Current (WSC) carrying AW into the Arctic Ocean, in proximity to the origin of the Fram Strait branch of AW circulation in the EB. Here, we used observations collected during 1997-2015 with several periods with missing data.

North of Svalbard (81°30'N, 31°00'E), moorings covering the Fram Strait inflow branch of the WSC over the upper part of the continental slope have been maintained since 2004 (*51*). The core of the inner branch of the WSC extends over bottom depths of around 500-1500 m and the moorings used in the present study have been positioned over depths between 850 and 1180 m.

Ice Tethered Profiler Observations

ITP buoys (*3,23*) (www.whoi.edu/itp) provided twice-daily CTD profiles in the upper ~750 m of the EB. The ITP CTDs were equipped with SBE-41/41CP CTD sensors and had high vertical resolution (25 cm or better) and accuracy of temperature 0.002°C and salinity 0.002. Data processing procedures are described at: http://www.whoi.edu/fileserver.do?id=35803&pt=2&p=41486. In our analysis we used data interpolated to a 25 cm fixed vertical grid; i.e., close to the original sampling interval. The time intervals covered by buoy measurements are shown by horizontal axes in Fig. 3b-d.

Fast-Ice Data

Fast-ice thickness observations at polar stations are conducted in winter by direct measurements of ice thickness at the same locations each year through the hole in ice using a ruler. Maximum thickness reached by seasonal ice in each year was used in this study to compose local and regional time series.

Atmospheric Data

De-seasoned monthly 2 m air temperatures from the European Centre for Medium-Range Weather Forecasts reanalysis ERA-Interim were used to complement station-based monthly mean temperature records in the Laptev Sea region (stations Kotelnii and Cheluskin) and expand the analysis to the eastern EB (Supplementary Materials Fig. S1).

Ekman Pumping

Ekman pumping velocity, w_e (m s^{-1}), is given by:

$$w_e = \frac{1}{\rho_o f}[\nabla \times \tau],$$

where τ is the surface wind stress, ρ_o = 1027 kg m^{-3} is the density of water, $f = 2\omega \cdot \sin\varphi$ is the Coriolis parameter, φ is latitude. Time series of wind stress were derived from ERA Interim Reanalysis sea level pressure by calculating geostrophic wind speed U (the area within 250km of 84^{o}N, 125^{o}E) and using the following empirical formula:

$$\tau = \rho_a C_D U |U|$$

where $C_D = 1.2\times10^{-3}$ is empirical constant and ρ_a = 1.29 kg m^{-3} is air density. Positive (negative) values represent cyclonic (anticyclonic) wind stress exerted on the surface causing a confluence (diffluence) of surface waters resulting in upwelling (downwelling) processes. Calculations of w_e were made without taking into account effects of ice. It has been shown that for the eastern EB, these effects are generally small; moreover, they tend to reduce the effect of wind (*14*).

Wavelet Analysis

Amplitudes and phases of seasonal signal were estimated using wavelet transformation of time series. Standard package of wavelet programs is used for

calculation of wavelet transforms based on the DOG Mother function (*53*). 95% confidence intervals and cones of influence shown in wavelet presentations are provided by the same package.

Definition of the Depth of the SML and CHL

We identify the depth of the SML by a change in water density from the ocean surface of 0.125 kg/m^3, following Ref. *54*. The lower CHL boundary is defined following *ref. 55* where an extensive collection of modern data was used and it was argued that the density ratio $R_\rho = (\alpha\partial\theta/\partial z)/(\beta\partial S/\partial z) = 0.05$ (α is the thermal expansion coefficient and β is the haline contraction coefficient, θ is potential temperature and S is salinity) may be used to establish the depth of the CHL base.

Definition of Heat Content Q

We quantify the changes in the CHL using vertically integrated heat content Q (J/m^2), defined as

$$Q = \int_{z_1}^{z_2} \rho_w c_p (\theta - \theta_{freezing}) dz,$$

where, $\theta_{freezing}$ is the freezing temperature ($-0.054 \cdot S$ may serve as a good proxy for the freezing point temperature), ρ_w is water density, c_p is specific heat of seawater and z_1 and z_2 are depths of the upper and lower boundaries. In physical terms, Q may be interpreted as the relative heat content, measuring how much heat must be removed to form ice crystals at a particular salinity and pressure.

Definition of Divergent Heat Flux F_h

We describe divergence of vertical heat flux F_h as the difference of diapycnal heat fluxes F_h at two depth levels. F_h is estimated from changes in time of vertically integrated heat content ΔQ. Note that these values are flux *differences*, and total heat fluxes may be larger than these values due to additional non-divergent heat transports (thus, our inferred estimates of heat fluxes represent *lower* bound for the total heat flux). For details, see *Ref. 14*.

Definition of the Layer for Estimates of Q and F_h

For the upper boundary of the layer, for which Q is estimated, we selected the depth 65 m, chosen because this best determines the layer in which heat from the AW is stored and released (*14*). The depth of winter ventilation H_{vent} is defined using an assumption that, starting from this depth, changes of water properties are not directly linked to the surface processes so that, for example, increase of depth of integration for calculation of Q beyond H_{vent} would not lead to statistically significant change of Q. Following this assumption, we calculated seasonal trends of Q gradually increasing the thickness of the layer for which Q is defined. Estimates of trends are shown in Supplementary Materials Table S1. Trends at the deepest layer, at which they are statistically different from the shallower-layer trends, are shown in bold.

Based on these estimates, we selected 130m as the boundary of the winter ventilation layer. As Table S1 shows, the boundary of the layer at M3e mooring is deeper, at ~150m. Therefore, our choice of H_{vent} is conservative (i.e. estimates of heat fluxes F_h derived from ΔQ would represent the lower bound) which is well justified considering the objectives of the study. Sensitivity of our estimates to the choice of H_{vent} is evaluated

calculating trends of ΔQ (and, therefore F_h) for 65-130m and 65-125m layers. These estimates showed that the 5m increase of the layer thickness increases F_h by 9%, which may be considered as an acceptable range of uncertainty. Therefore, for all moorings Q and their trends (and therefore F_h) are estimated using a 65-130m depth interval.

Supplementary Text

Supplementary Materials References

51. V. V. Ivanov *et al*., *Deep-Sea Res*. I. **56**, 1-14 (2009).

52. Polyakov, I. V. *NSF Arctic Data Center*. arctic-data.7792.16 (2016).

53. C. Torrence, G. P. Compo, *Bull. Amer. Meteor. Soc.* **79**(1), 61-78 (1998).

54. G. Monterey, S. Levitus, S. NOAA Atlas NESDIS 14, U.S. Gov. Printing Office, Wash., D.C., 96 pp (1997).

55. P. Bourgain, J.-C. Gascard, *Deep-Sea Res. I*, **58**, 745-756 (2011).

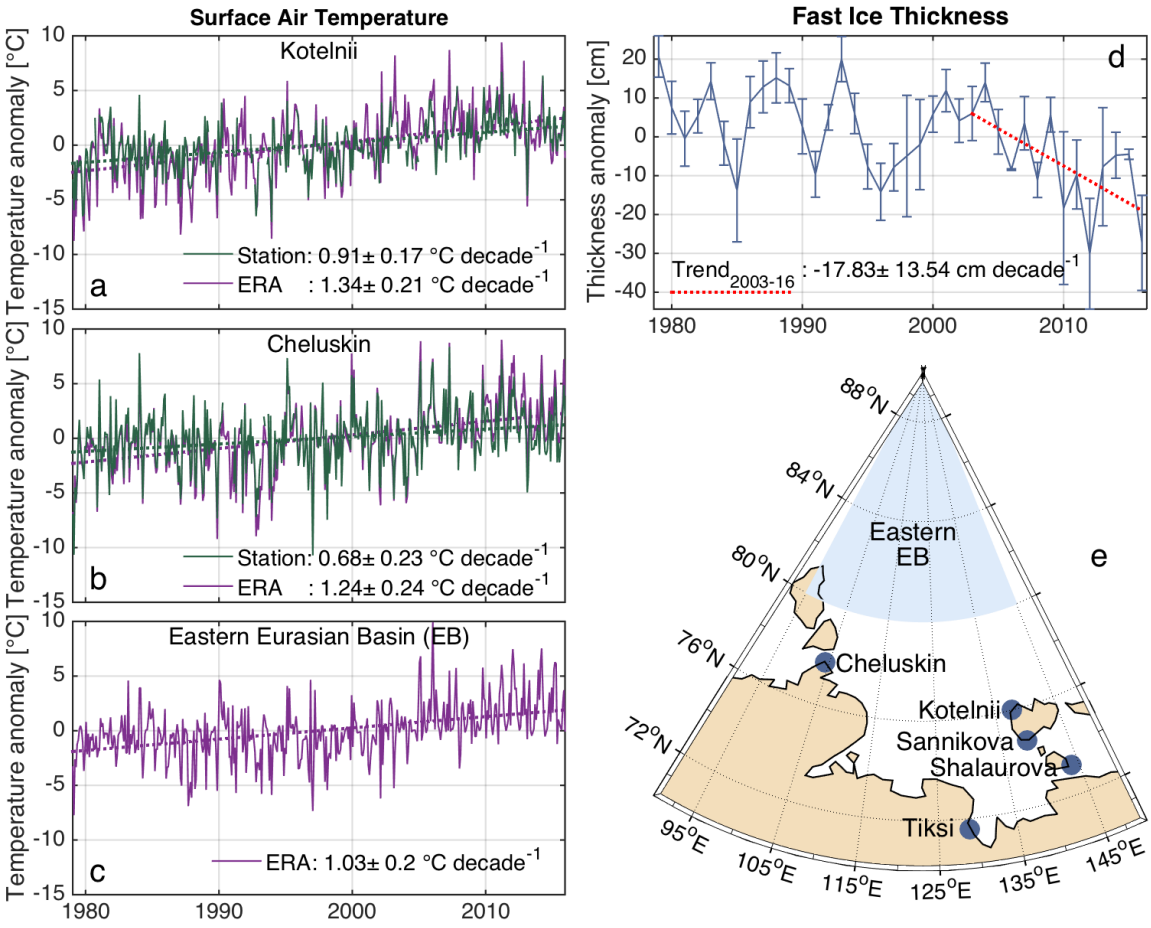

Fig. S1.

(a-c) Monthly surface air temperature (SAT) anomalies (°C) and their trends, from two polar stations (a, b) and the ERA-Interim reanalysis product (a-c). (d) Fast-ice thickness anomalies (cm) and their trend over 2003-2016, and (e) map showing locations of stations providing air temperature and fast-ice thickness observations; blue color is used to indicate the region used for calculation of area-averaged SAT time series for the eastern EB shown in (c).

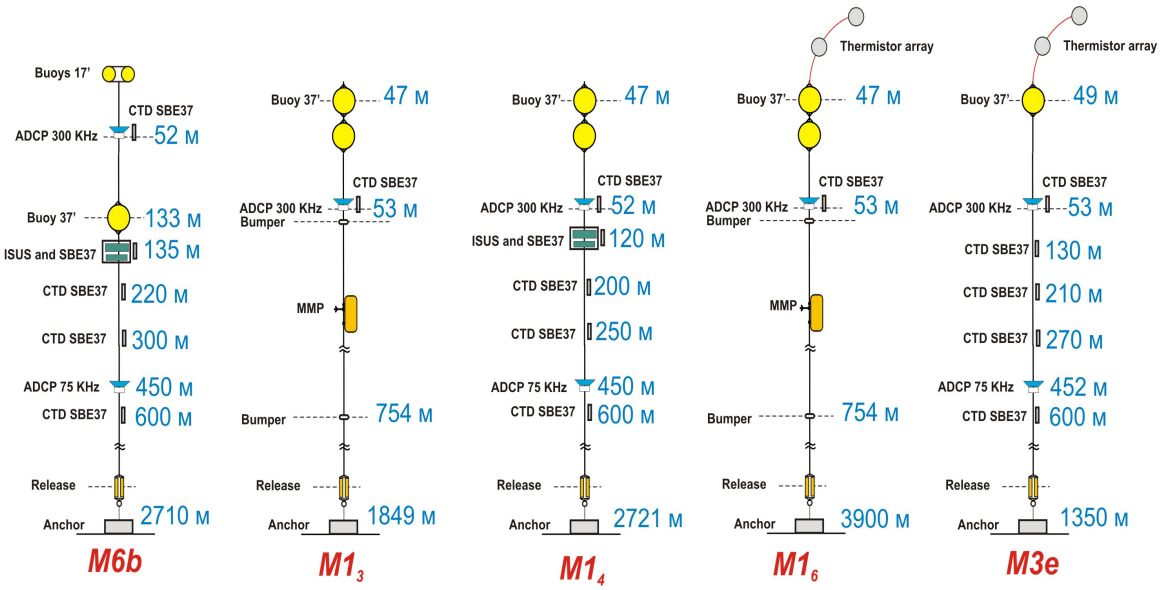

Fig. S2.

Schematics of moorings used in this study. Abbreviations used in this figure and relevant to our discussions are: CTD = Conductivity-Temperature-Depth, ADCP = Acoustic Doppler Current Profiler, MMP = McLane Moored Profiler. Thermistor arrays included two SBE-37 and several SBE-56 separated by 2m intervals and provided temperature records only.

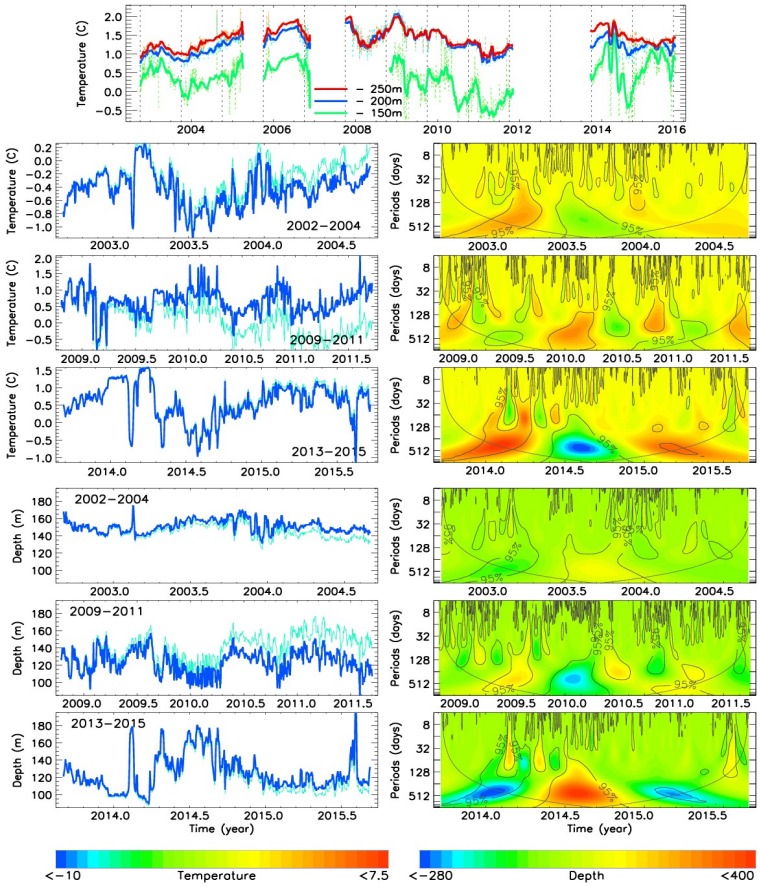

Fig. S3.

Time series and their wavelet transforms from the Laptev Sea mooring site $M1_4$, eastern Eurasian Basin of the Arctic Ocean (φ = 78° 27.5' N, λ = 125° 53.7' E). In panels with wavelet transforms, statistical significance and cones of influence are shown by grey lines. (Top) Composite time series of water temperature at three depth levels. Dotted lines show daily time series and solid lines show monthly mean time series. Note enhanced seasonal signal in winters of 2013/14 and 2014/15. White segments indicate missing data. (Next three rows) Original (light blue) and de-trended (dark blue) time series of water temperature measured at 150m (left) and wavelet transforms of de-trended time series (right). Note the strongest seasonal signal in the last two years.
(Bottom three rows) Original (light blue) and de-trended (dark blue) time series of the upper Atlantic Water (AW) boundary (defined by 0^{o}C isotherm, left) and wavelet transforms of de-trended time series (right). Note: a) Strongly amplified seasonal signal in the recent years and b) extreme shoaling of the AW layer in winters of 2013/14 and 2014/15.

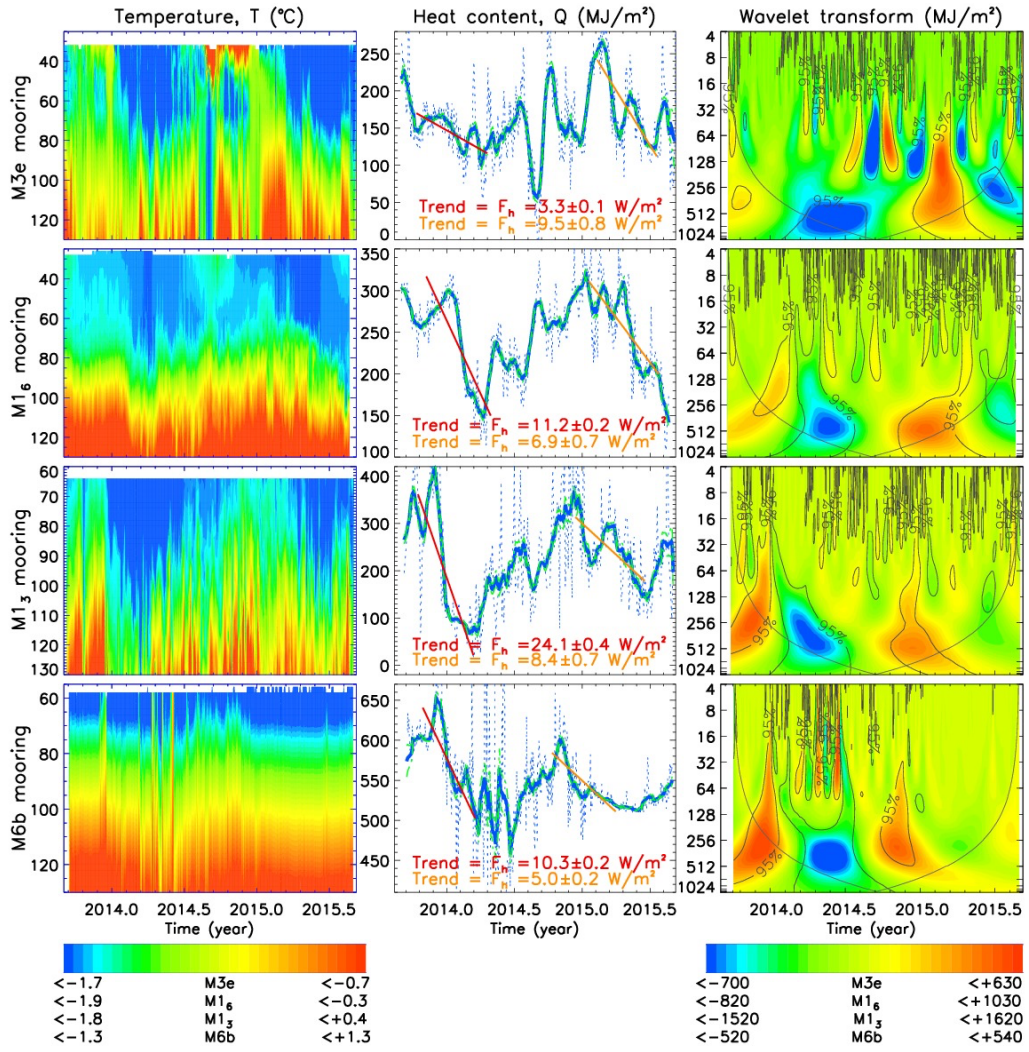

709

710

711 **Fig. S4.**

712 (left) Depth (m, vertical axes) versus time of water temperature, (middle) time series of *Q*
713 for the 65-130m layer (dotted blue lines show daily series, solid blue lines show monthly
714 means and green dashed line show standard errors) and (right) wavelet transforms of the
715 time series of *Q* for four moorings. Maxima and minima of wavelet transforms were used
716 to define the boundary of winter seasons. These boundaries were used to calculate trends
717 of *Q* shown by red (winter 2013/14) and orange (winter 2014/15) lines. Slope of trends
718 defines the rate of change of *Q* in time, which is equivalent to the divergent heat flux F_h
719 (shown in red and orange).

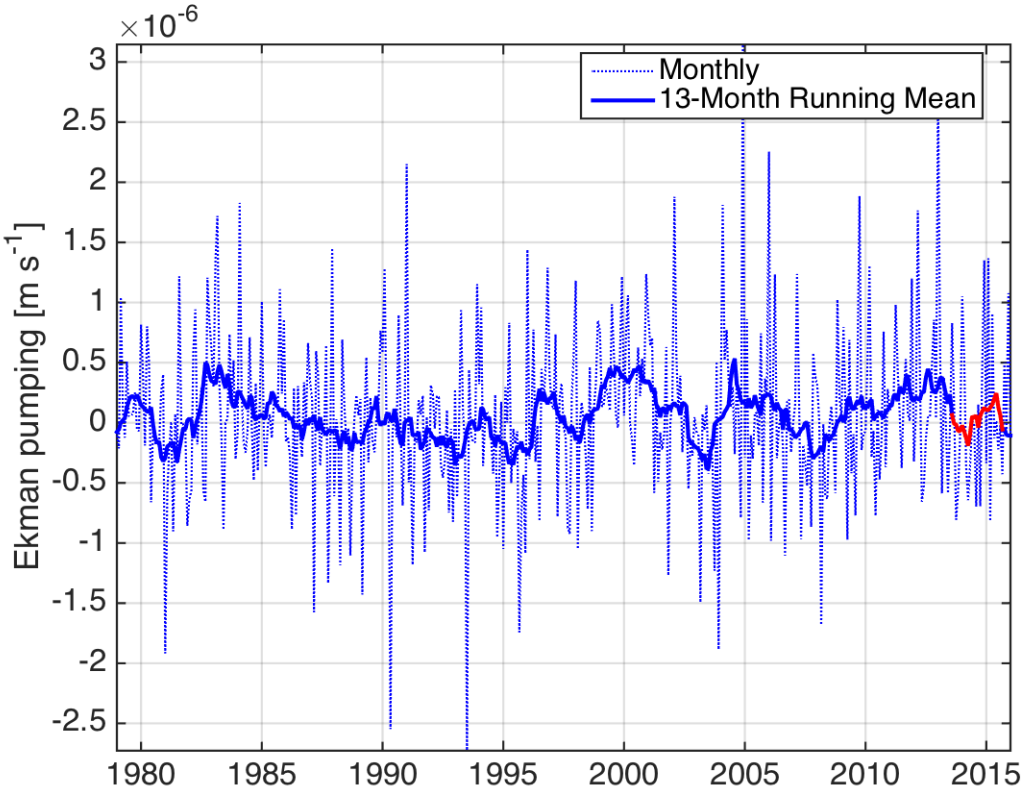

720

721 **Fig. S5.**

722 Time series of Ekman pumping velocity w_e averaged over the eastern EB of the Arctic
723 Ocean (see definition of the area in Supplementary Materials Fig. S4; positive is
724 upwelling, negative is downwelling). Red segment of the time series shows w_e for the
725 period of time covered by mooring observations; weak velocities suggest negligible role
726 of Ekman pumping in AW shoaling.

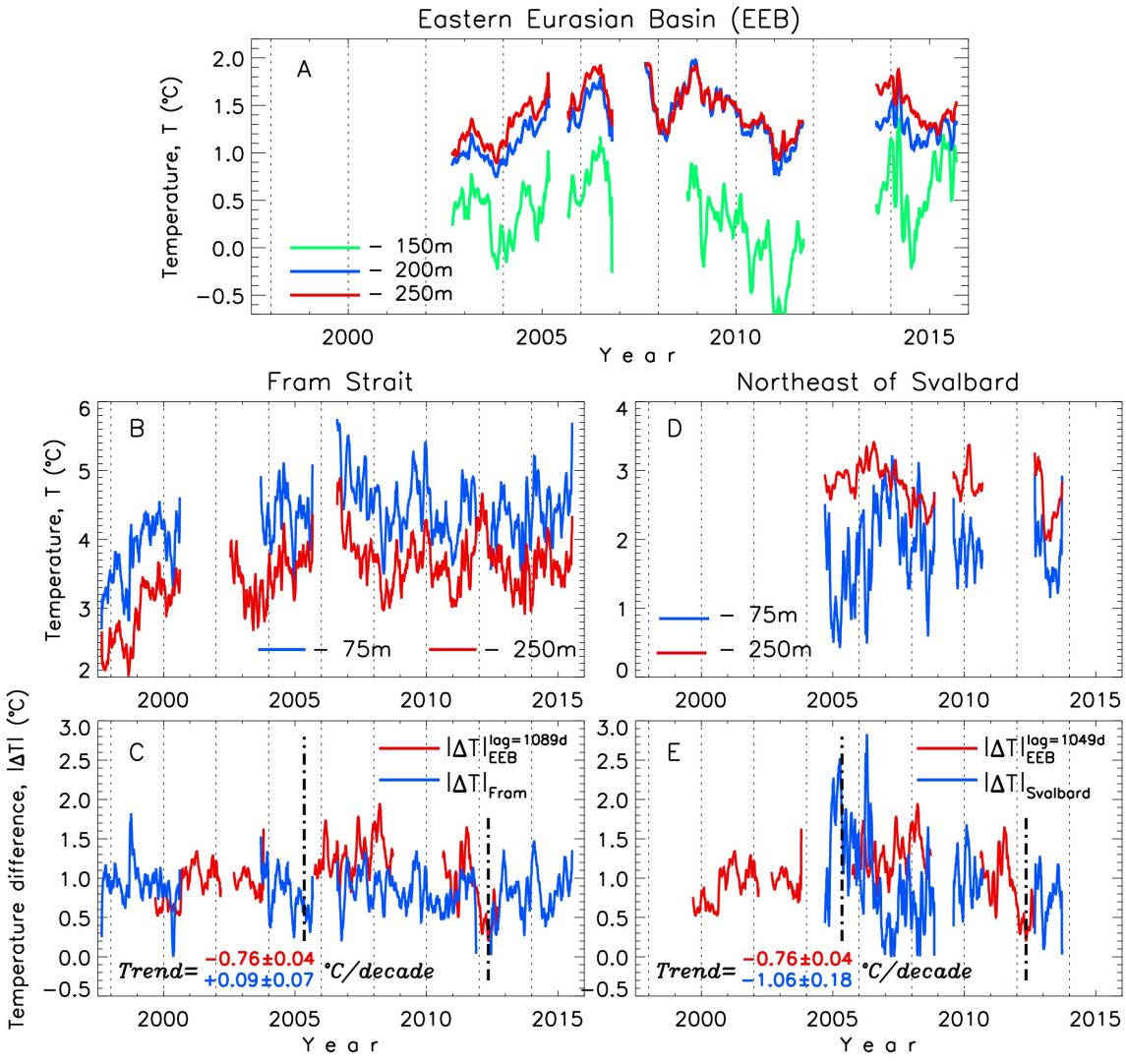

Fig. S6.

De-seasoned time series of AW temperatures (°C) in the eastern EB (A), Fram Strait (B) and northeast of Svalbard (D) smoothed using 30-days running mean smoothing window and corresponding temperature differences (C, E). Vertical dash-dotted lines in C, E identify segments of the records corresponding to intensive loss of temperature contrast between the upper and lower water layers; trends are computed for these segments. Lags (C,E) are defined using correlation analysis. White segments indicate missing data.

737 **Table S1.**

738 Estimates of winter 2014/15 trends of Q [W m^{-2}].

Layer (meters)	***Moorings***			
	M3e	**M1$_6$**	**M1$_3$**	**M6b**
65-100	5.02±0.40	3.95±0.38	5.01±0.32	3.68±0.15
65-110	6.48±0.49	5.03±0.50	6.53±0.46	4.30±0.19
65-120	7.97±0.75	6.07±0.61	7.48±0.59	4.73±0.22
65-130	9.47±0.75	**6.90±0.69**	**8.39±0.74**	**4.98±0.25**
65-140	11.00±0.91	7.52±0.75	8.91±0.87	5.16±0.28
65-150	**12.43±1.05**			
65-160	13.45±1.17			

739

740

741